Int. J. Solids Structures Vol. 30, No. 1, pp. 137–149, 1993
Printed in Great Britain.

0020–7683/93 $5.00+ .00

FAILURE ANALYSIS OF AIRCRAFT ENGINE DISKS

M. KÖHL and G. DHONDT
Motoren- und Turbinen-Union München GmbH, Abt. EMBM, Dachauer Straße 665,
8000 München 50, Germany

(*Received* 3 *September* 1991)

Abstract—This paper is concerned with an estimate of the size of the resulting engine disk fragments after failure due to radial cracking. The disk is modelled by a rotating ring in which the stress history after cracking is calculated. The results show that immediately after failure bending moments and normal forces propagate away from the crack region while increasing. However, arriving at about 100–130° away from the crack surfaces the propagation speed of the maximum bending moment and normal forces noticeably decreases, though their value is still strongly increasing.

An exceeding of the ultimate tensile strength in this situation leads to a second failure at about 120° away from the original crack.

The resultant fragments, each of them approximately one third of the original disk, have the biggest translational energy of all possible failure modes.

1. INTRODUCTION

Experience has shown that disks often break into three parts of approximately the same size. In this paper the stress pattern after a radial failure of the disk is calculated by modal analysis. It is shown that this stress distribution can lead to an additional failure at about 120° away from the original crack surface. A numerical example is given with data from a real existing, though simplified, aircraft engine disk.

2. ENERGY CONSIDERATIONS

The damage due to a disk fragment, broken away from a rotating disk, is mainly determined by its translational energy (McCarthy, 1975). For the disk section in Fig. 1 with thickness d, density ρ, opening angle α, inner radius r_i and outer radius r_o, the mass $M(\alpha)$ can be written as

$$M(\alpha) = \rho \cdot \tfrac{1}{2}(r_o^2 - r_i^2)\alpha \cdot d, \tag{1}$$

and the radius of the centre of gravity is

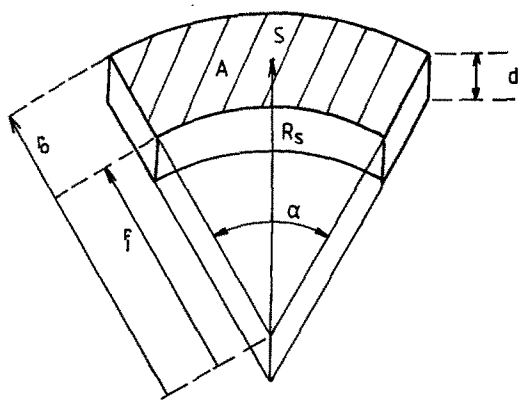

Fig. 1. Disk section.

$$R_s(\alpha) = \frac{4(r_o^3 - r_i^3)\sin \alpha/2}{3(r_o^2 - r_i^2)\alpha}. \tag{2}$$

This leads to the translational kinetic energy $E_t(\alpha)$:

$$E_t(\alpha) = \tfrac{1}{2}M(\alpha)R_s^2(\alpha)\omega^2, \tag{3}$$

where ω is the rotational speed of the fragment before breaking away. From (1), (2) and (3) the dependence of E_t on α is

$$E_t(\alpha) \propto \frac{1}{\alpha}\sin^2\frac{\alpha}{2}. \tag{4}$$

E_t has a maximum for

$$\alpha = \tan(\alpha/2) \tag{5}$$

or

$$\alpha = 133.6°. \tag{6}$$

Figure 2 shows E_t as a function of α. The curve is very flat in the neighbourhood of its maximum. Given that we are interested in all fragments for which

$$E_t > 0.95(E_t)_{max}, \tag{7}$$

the applicable range of α is

$$105° < \alpha < 163°. \tag{8}$$

In the following sections an estimate of the size of the fragments will be made, in order to check whether they satisfy (8).

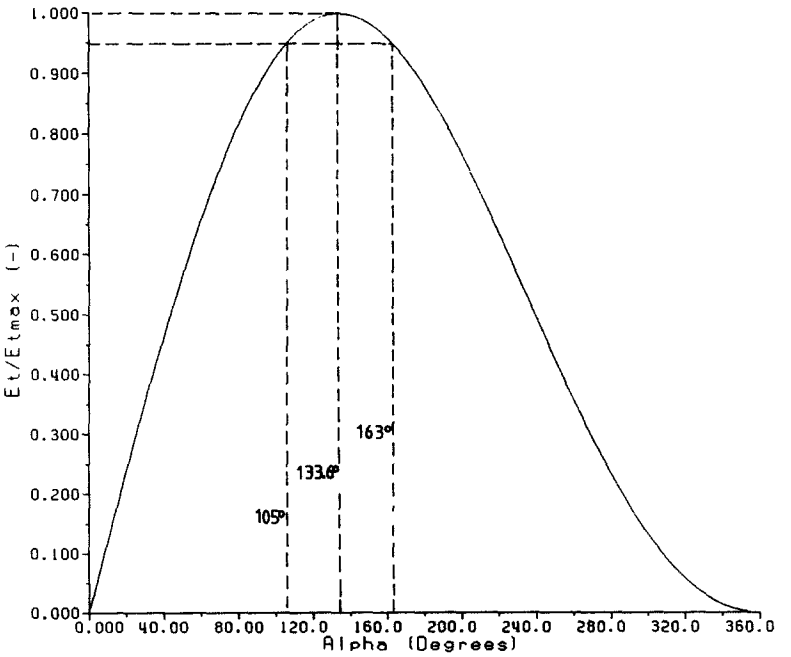

Fig. 2. Translational energy of a disk segment with angle α.

3. THE MODEL

The model for the disk is a rotating ring with constant section (Fig. 3). Because of the symmetry conditions only half the disk has to be modelled. The geometry of the ring can be written as (Fig. 4)

$$r(\varphi) = R+u(\varphi), \tag{9}$$

where R is the constant radius and $u(\varphi)$ is the radial displacement.

The external load q consists of centrifugal and inertial forces:

$$q = q_z - m\ddot{u}, \tag{10}$$

where $\ddot{u} = \partial^2 u/\partial t^2$.

Expressing the equilibrium conditions for a fragment between $\psi = 0$ and $\psi = \varphi$ leads to (Fig. 5):

$$M(\varphi, t) = \int_{\psi=0}^{\varphi} q \cdot R^2 \cdot \sin(\varphi-\psi)\,\mathrm{d}\psi, \tag{11}$$

$$N(\varphi, t) = \int_{\psi=0}^{\varphi} q \cdot R \cdot \sin(\varphi-\psi)\,\mathrm{d}\psi, \tag{12}$$

$$Q(\varphi, t) = \int_{\psi=0}^{\varphi} q \cdot R \cdot \cos(\varphi-\psi)\,\mathrm{d}\psi. \tag{13}$$

M is the bending moment, N the normal force and Q the shear force. Substituting (10) in (11) and comparing (11), (12) and (13) one gets:

$$M(\varphi, t) = q_z R^2(1-\cos\varphi) - mR^2 \int_{\psi=0}^{\varphi} \ddot{u}(\psi)\sin(\varphi-\psi)\,\mathrm{d}\psi, \tag{14}$$

$$N(\varphi, t) = M(\varphi, t)/R, \tag{15}$$

$$Q(\varphi, t) = -\frac{\partial N(\varphi, t)}{\partial \varphi}. \tag{16}$$

The first order relationship between the bending moment and the displacements for a ring is (Szabó, 1964):

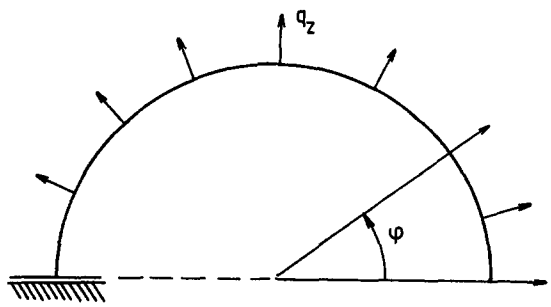

Fig. 3. Model of the disk.

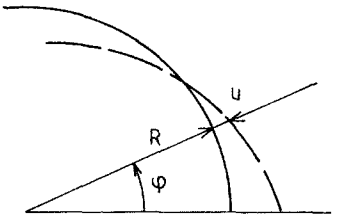

Fig. 4. Deformation of the disk.

$$u''(\varphi)+u(\varphi)=\frac{R^2}{EI}M(\varphi), \tag{17}$$

where E is Young's Modulus, $u''(\varphi):=\partial^2 u/\partial\varphi^2$ and I is the moment of inertia of the cross-section of the ring. Substitution of (17) into (11) yields the governing equation:

$$u''(\varphi,t)+u(\varphi,t)+\frac{mR^4}{EI}\int_{\psi=0}^{\varphi}\ddot{u}(\psi,t)\sin(\varphi-\psi)\,d\psi=\frac{q_z R^4}{EI}(1-\cos\varphi). \tag{18}$$

Up to $t=0$ the disk is uncracked, so the initial conditions are:

$$u(\varphi,0)=\dot{u}(\varphi,0)=0 \quad \text{for all } \varphi\in[0,\pi]. \tag{19}$$

The boundary conditions for $t\geqslant 0$ (i.e. after cracking) are:

(1) $\varphi=0$ is a free end, hence

$$M(0,t)=N(0,t)=Q(0,t)=0. \tag{20}$$

These conditions are already satisfied by (18).

(2) $\varphi=\pi$ is a symmetry plane:

$$u'(\pi,t)=Q(\pi,t)=0. \tag{21}$$

Combining (15), (16) and (17), (21) is equivalent with

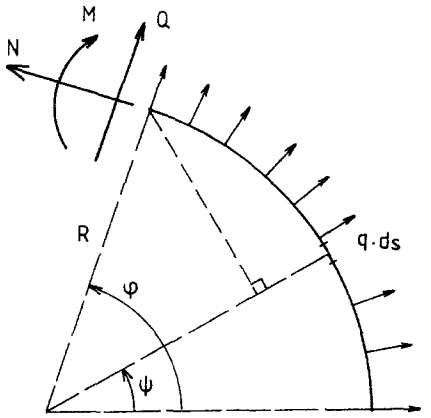

Fig. 5. Internal forces in the disk.

$$u'(\pi, t) = u'''(\pi, t) = 0, \quad (t \geqslant 0). \tag{22}$$

4. MODAL ANALYSIS

Consider the homogeneous equation of the problem:

$$u''(\varphi, t) + u(\varphi, t) + \frac{mR^4}{EI} \int_{\psi=0}^{\varphi} \ddot{u}(\psi, t) \sin(\varphi - \psi)\, d\psi = 0. \tag{23}$$

Looking for a solution of the form

$$u(\varphi, t) = y(\varphi)\, e^{i\omega t} \tag{24}$$

and substituting this in (23) one gets

$$y''(\varphi) + y(\varphi) - \frac{mR^4\omega^2}{EI} \int_{\psi=0}^{\varphi} y(\psi) \sin(\varphi - \psi)\, d\psi = 0 \tag{25}$$

and the boundary conditions are

$$y'(\pi) = y'''(\pi) = 0. \tag{26}$$

Taking the Laplace transform of (25) yields:

$$Y(s) = \frac{y(0)s^3 + y'(0)s^2 + y(0)s + y'(0)}{s^4 + 2s^2 + 1 - \lambda^2}, \tag{27}$$

with

$$Y(S) = \int_{\varphi=0}^{\infty} e^{-s\varphi}\, y(\varphi)\, d\varphi \tag{28}$$

and

$$\lambda^2 := \frac{mR^4\omega^2}{EI}. \tag{29}$$

The poles of $Y(s)$ are

$$s_{1,2} = \pm\sqrt{\lambda - 1}; \quad s_{3,4} = \pm i\sqrt{\lambda + 1}. \tag{30}$$

Applying the inverse transform to (27), $y(\varphi)$ takes the form:

$$y(\varphi) = \sum_{i=1}^{4} A_i e^{s_i\varphi}, \tag{31}$$

$$A_i = \frac{1}{4}\left(y(0) + \frac{y'(0)}{s_i}\right), \quad i = 1, 4 \tag{32}$$

or

$$y(\varphi) = \frac{1}{2}\Big[y(0)(\cosh(\sqrt{\lambda-1}\varphi)+\cos(\sqrt{\lambda+1}\varphi))+y'(0)\Big(\frac{1}{\sqrt{\lambda-1}}\sinh(\sqrt{\lambda-1}\varphi) + \frac{1}{\sqrt{\lambda+1}}\sin(\sqrt{\lambda+1}\varphi)\Big)\Big]. \quad (33)$$

Taking the boundary conditions (26) into account yields a nontrivial solution only if:

$$\sqrt{1+\lambda}\cdot\tan(\sqrt{1+\lambda}\pi) = \sqrt{1-\lambda}\cdot\tan(\sqrt{1-\lambda}\pi), \quad \text{for } \lambda < 1 \quad (34)$$

$$= -\sqrt{\lambda-1}\cdot\tanh(\sqrt{\lambda-1}\pi), \quad \text{for } \lambda > 1. \quad (35)$$

$\lambda = 0$ corresponds to a rigid body motion and is of no further interest. $\lambda = 1$ is not an eigenvalue. The first 10 eigenvalues are given in Table 1. For $\lambda \gg 1$ one can use the following approximations:

$$\sqrt{\lambda+1} \simeq \sqrt{\lambda-1} \simeq \sqrt{\lambda}, \quad \lambda \to +\infty \quad (36)$$

and

$$\tanh(\sqrt{\lambda-1}\pi) \simeq 1, \quad \lambda \to +\infty \quad (37)$$

and so (35) reduces to

$$\tan(\sqrt{1+\lambda}\pi) = -1 \quad (38)$$

with the solution:

$$\lambda_j = (j-1/4)^2 - 1. \quad (39)$$

Table 1 shows that (39) is a very good approximation for $j \geqslant 4$. Substitution of the eigenvalues in (33) and expressing $y(0)$ as a function of $y'(0)$ by means of the boundary conditions (26), one gets the eigenmodes:

$$y_j(\varphi) = C\Big[\cos(\sqrt{1-\lambda_j}\cdot\varphi)+\cos(\sqrt{1+\lambda_j}\cdot\varphi) - Q_j\Big(\frac{\sin(\sqrt{1-\lambda_j}\varphi)}{\sqrt{1-\lambda_j}} + \frac{\sin(\sqrt{1+\lambda_j}\varphi)}{\sqrt{1+\lambda_j}}\Big)\Big], \quad \lambda_j < 1. \quad (40)$$

Table 1

Mode j	Exact eigenvalues λ_j	Approximated eigenvalues λ_j	Error of approximated eigenvalues [eqn (39)] [%]	Max. error of approximated eigenmodes [%]
1	0.8029	—	—	—
2	2.3169	2.0625	−10.980	1.900
3	6.6943	6.5625	−1.969	0.038
4	13.1535	13.0625	−0.692	0.001
5	21.6325	21.5625	−0.324	0.000
6	32.1195	32.0625	−0.177	0.000
7	44.6107	44.5625	−0.108	0.000
8	59.1042	59.0625	−0.071	0.000
9	75.5993	75.5625	−0.049	0.000
10	94.0955	94.0625	−0.035	0.000

$$y_j(\varphi) = C\Big[\cosh\left(\sqrt{\lambda_j-1}\varphi\right)+\cos\left(\sqrt{1+\lambda_j}\varphi\right) - Q_j\left(\frac{\sinh\left(\sqrt{\lambda_j-1}\varphi\right)}{\sqrt{\lambda_j-1}}+\frac{\sin\left(\sqrt{1+\lambda_j}\varphi\right)}{\sqrt{1+\lambda_j}}\right)\Big], \quad \lambda_j > 1, \quad (41)$$

with

$$Q_j := -\frac{\sqrt{1-\lambda_j}\sin\left(\sqrt{1-\lambda_j}\pi\right)+\sqrt{1+\lambda_j}\sin\left(\sqrt{1+\lambda_j}\pi\right)}{\cos\left(\sqrt{1-\lambda_j}\pi\right)+\cos\left(\sqrt{1+\lambda_j}\pi\right)}, \quad \lambda_j < 1, \quad (42)$$

$$Q_j := \frac{\sqrt{\lambda_j-1}\sinh\left(\sqrt{\lambda_j-1}\pi\right)-\sqrt{1+\lambda_j}\sin\left(\sqrt{1+\lambda_j}\pi\right)}{\cosh\left(\sqrt{\lambda_j-1}\pi\right)+\cos\left(\sqrt{1+\lambda_j}\pi\right)}, \quad \lambda_j > 1. \quad (43)$$

C is an arbitrary constant.

For $\lambda_j \gg 1$ the evaluation of (41) causes some numerical problems because of the subtraction of very large numbers, yielding a result which is several orders of magnitude smaller. For that case an asymptotic expansion has been derived:

$$y_j(\varphi) \simeq \cos\left(\sqrt{\lambda_j+1}\varphi\right)-\sqrt{\frac{\lambda_j-1}{\lambda_j+1}}\sin\left(\sqrt{\lambda_j+1}\varphi\right)+\exp\left(-\sqrt{\lambda_j-1}\varphi\right) + \left[\cos\left(\sqrt{\lambda_j+1}\pi\right)+\sqrt{\frac{\lambda_j+1}{\lambda_j-1}}\sin\left(\sqrt{\lambda_j+1}\pi\right)\right]\exp\left[-\sqrt{\lambda_j-1}(\pi-\varphi)\right], \quad \lambda_j \to +\infty, \quad \varphi \neq 0. \quad (44)$$

This follows from (41) and (43) by taking into account that:

$$\frac{1}{\cosh\left(\sqrt{\lambda_j-1}\pi\right)+\cos\left(\sqrt{\lambda_j+1}\pi\right)} \simeq \frac{1}{\cosh\left(\sqrt{\lambda_j-1}\pi\right)}\cdot\left\{1-\frac{\cos\left(\sqrt{\lambda_j+1}\pi\right)}{\cosh\left(\sqrt{\lambda_j-1}\pi\right)}\right\}, \quad \lambda_j \to +\infty \quad (45)$$

and

$$\frac{\sinh\left(\sqrt{\lambda_j-1}\varphi\right)}{\cosh\left(\sqrt{\lambda_j-1}\pi\right)} \simeq \exp\left(\sqrt{\lambda_j-1}(\varphi-\pi)\right), \quad \lambda_j \to +\infty, \quad \varphi \neq 0. \quad (46)$$

The bending moments and normal forces corresponding to the first five eigenvalues are given in Fig. 6 and are found by (15) and (17):

$$M_j(\varphi) = RN_j(\varphi) = \frac{EI}{R^2}\left(y_j''(\varphi)+y_j(\varphi)\right). \quad (47)$$

The internal forces for the static case

$$M_s(\varphi) = RN_s(\varphi) = q_z R^2(1-\cos\varphi) \quad (48)$$

have also been included. All curves are normalized.

The quality of the asymptotic eigenmode expansion (44) is illustrated in Table 1, where the maximum error over φ, referred to the amplitude of the respective exact eigenmode, is

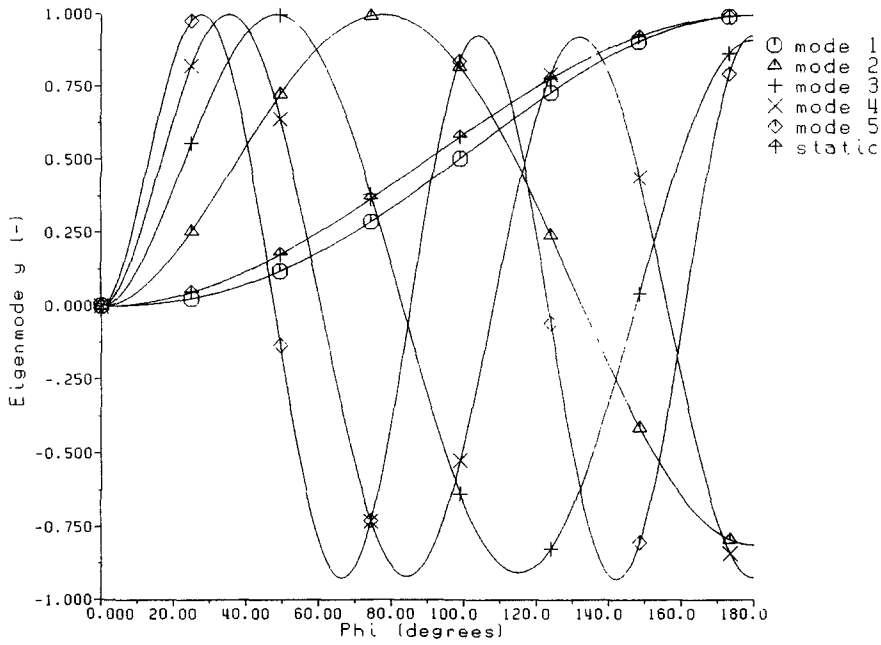

Fig. 6. Normalized eigenfunctions of the bending moment.

presented for modes 2–10. The error values show that the asymptotic expansion is extremely good even for modes as small as $j = 3$.

5. SOLUTION OF THE INSTATIONARY INHOMOGENEOUS PROBLEM

To solve the original equation (18), we transform it by taking the second derivative with respect to φ and adding it to (18). The result is a fourth-order partial differential equation:

$$u'''' + 2u'' + u + \frac{mR^4}{EI}\ddot{u} = \frac{q_z R^4}{EI}. \tag{49}$$

The solution $u(\varphi, t)$ is expanded in the eigenfunctions:

$$u(\varphi, t) = \sum_{j=1}^{\infty} c_j(t) y_j(\varphi) \tag{50}$$

with time dependent coefficients $c_j(t)$.

Substitution of (50) into (49) yields:

$$\sum_{j=1}^{\infty} \left[c_j(t)(y_j'''' + 2y_j'' + y_j) + \ddot{c}_j(t) \frac{\lambda_j^2}{\omega_j^2} y_j \right] = \frac{q_z R^4}{EI} \tag{51}$$

with

$$\lambda_j^2 := \frac{mR^4 \omega_j^2}{EI}.$$

y_j is a solution of the homogeneous equation:

$$y_j'''' + 2y_j'' + y_j = \lambda_j^2 y_j, \tag{52}$$

and (51) can be transformed into:

$$\sum_{j=1}^{\infty} \left[\left(\ddot{c}_j(t) + \omega_j^2 c_j(t) \right) \frac{\lambda_j^2}{\omega_j^2} y_j(\varphi) \right] = \frac{q_z R^4}{EI}. \tag{53}$$

One can prove that the eigenvalue problem (52) with the boundary conditions (20) and (21) is self-adjoint. Hence the eigenfunctions are orthogonal towards each other

$$\int_0^{\pi} y_j(\varphi) y_k(\varphi) \, \mathrm{d}\varphi = 0, \quad \text{for } j \neq k. \tag{54}$$

By use of (54), (53) is transformed to:

$$\ddot{c}_j(t) + \omega_j^2 c_j(t) = \frac{q_z R^4 \omega_j^2 \int_0^{\pi} y_j \, \mathrm{d}\varphi}{EI\lambda_j^2 \int_0^{\pi} y_j^2 \, \mathrm{d}\varphi}. \tag{55}$$

Because of the independence of the eigenmodes, the initial conditions (19) are equivalent to:

$$c_j(0) = \dot{c}_j(0) = 0 \tag{56}$$

and the solution of (55) and (56) is:

$$c_j(t) = \frac{q_z R^4 \int_0^{\pi} y_j \, \mathrm{d}\varphi}{EI\lambda_j^2 \int_0^{\pi} y_j^2 \, \mathrm{d}\varphi} (1 - \cos \omega_j t). \tag{57}$$

Consequently the solution of (18) is:

$$\frac{M(\varphi, t)}{q_z R^2} = \frac{N(\varphi, t)}{q_z R} = \sum_{j=1}^{\infty} \frac{\int_{\psi=0}^{\pi} y_j \, \mathrm{d}\psi}{\lambda_j^2 \int_{\psi=0}^{\pi} y_j^2 \, \mathrm{d}\psi} (1 - \cos \omega_j t)\left(y_j(\varphi) + y_j''(\varphi) \right). \tag{58}$$

The shear forces are:

$$\frac{Q(\varphi, t)}{q_z R} = -\sum_{j=1}^{\infty} \frac{\int_{\psi=0}^{\pi} y_j \, \mathrm{d}\psi}{\lambda_j^2 \int_{\psi=0}^{\pi} y_j^2 \, \mathrm{d}\psi} (1 - \cos \omega_j t)\left(y_j'(\varphi) + y_j'''(\varphi) \right). \tag{59}$$

6. CALCULATION OF THE INTERNAL FORCES AFTER CRACKING

Since the bending moments and normal forces are linearly dependent, they can be represented by one function:

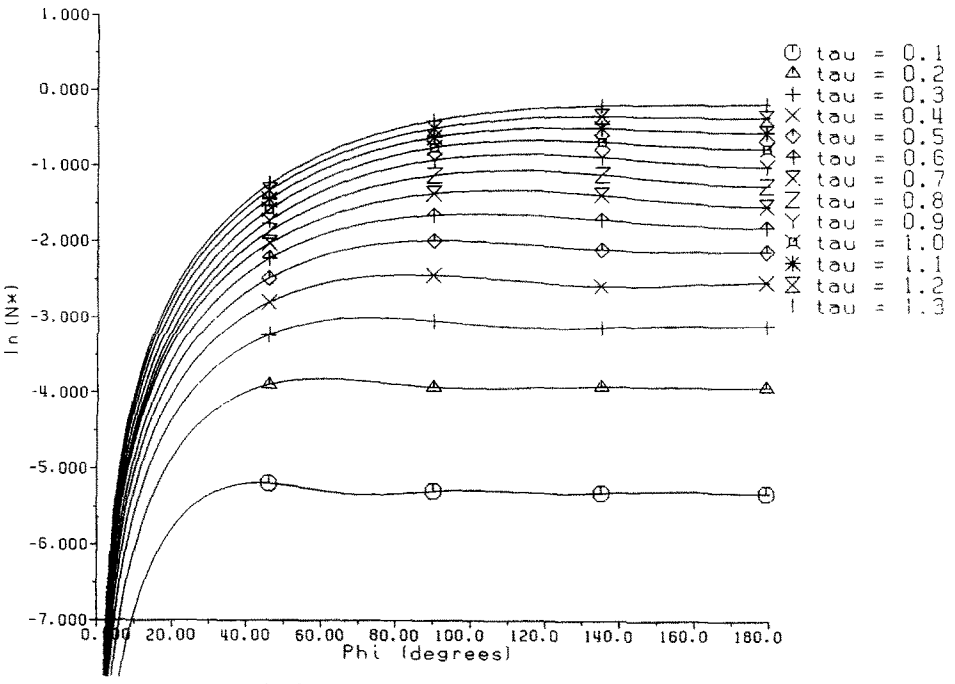

Fig. 7. Normalized normal forces at different times.

$$N^*(\varphi, t) := \frac{N(\varphi, t)}{q_z R} = \frac{M(\varphi, t)}{q_z R^2}. \tag{60}$$

The internal forces immediately after a radial failure has taken place ($t = 0$) are of special interest for our problem. Figure 7 shows N^* as a function of φ for different time values:

$$\tau := \frac{1}{R^2}\sqrt{\frac{EI}{m}} \cdot t \tag{61}$$

is introduced in order to produce material and geometry independent curves. At $t = 0+$ (i.e. immediately after cracking, $N^* = 0$) N^* increases for all φ and has a maximum along φ, which propagates away from the crack surfaces. Depending on the ultimate tensile strength of the material it could well happen that an additional failure occurs before this maximum reaches $\varphi = 180°$.

Figure 8 shows the maximum N^*_{max} of N^* over φ and the angle φ_{max} at which it occurs as a function of time. It reveals an additional phenomenon: at about $\varphi_{max} = 120°$, the propagation speed of N^*_{max} slows down significantly, while the value of N^*_{max} continues to increase strongly. This makes an additional failure in the region about $\varphi = 120°$ even more likely. This tendency is also confirmed by the $\varphi_{max} - N^*_{max}$ curve in Fig. 9. An exceeding of UTS (Ultimate Tensile Strength) in the range $0.22 \leqslant N^*_{max} \leqslant 0.82$ leads to a failure for $105° \leqslant \varphi \leqslant 163°$, and consequently to disk fragments with a high translational kinetic energy (cf. Section 2).

7. EXAMPLE

Figure 10 shows the simplified geometry of a real existing disk. The normal stresses have a maximum at the inner radius:

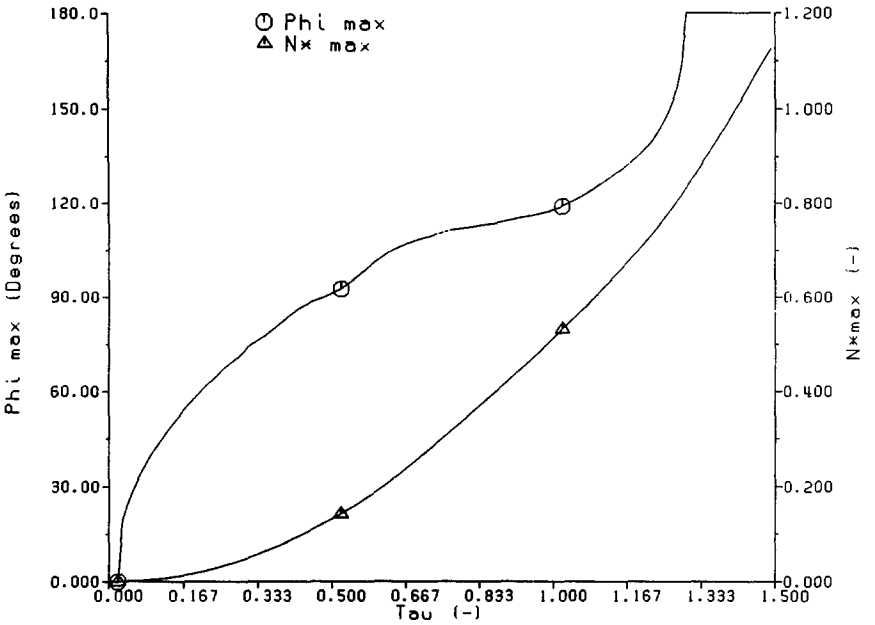

Fig. 8. Time dependence of the maximum normalized normal force N^*_{max} and of the corresponding angle φ_{max}.

$$\sigma_i = \frac{N}{A} + \alpha_{ki}\frac{M}{W_i} \tag{62}$$

with

$$W_i = \frac{1}{R_s - R_i}\int_{r=R_i}^{R_o} (r - R_s)^2 t(r)\,dr. \tag{63}$$

A is the area of the cross-section, R_s is the radius of the centre of gravity and α_{ki} is a parameter which depends on the curvature of the ring (Beitz and Küttner, 1983).

Substituting (60) into (62) for $R = R_s$, one finds

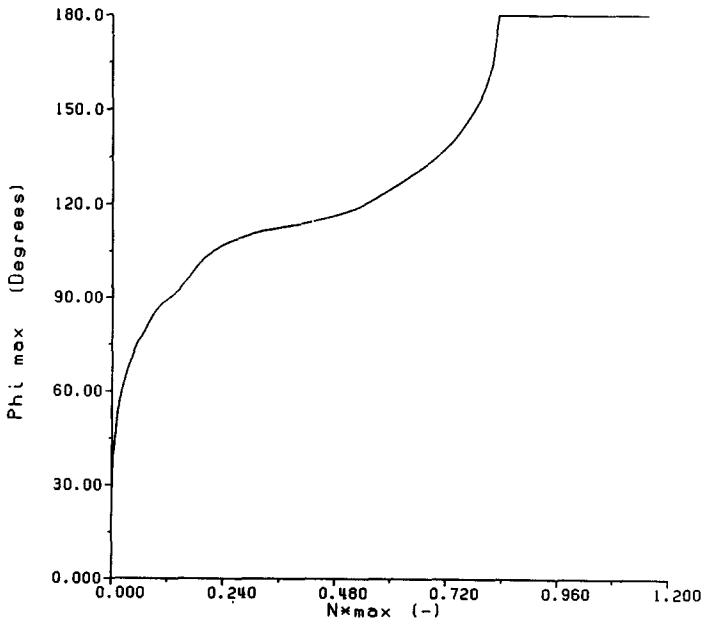

Fig. 9. Angle φ_{max} for which the maximum normal force occurs, as a function of N^*_{max}.

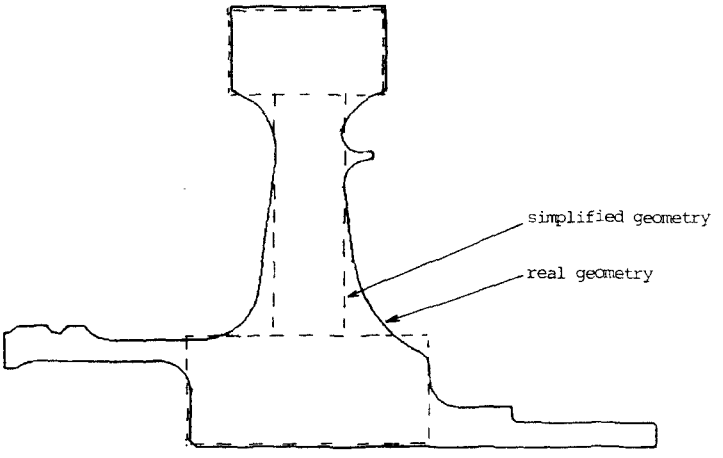

Fig. 10. Example of disk geometry.

$$\sigma_t = N^* q_z R_s \left(\frac{1}{A} + \alpha_{ki} \frac{R_s}{W_t} \right), \tag{64}$$

where q_z is the centrifugal load per unit length:

$$q_z = 2\pi f^2 \rho V, \tag{65}$$

with f the frequency, ρ the density and V the total volume of the disk.

For the disk in Fig. 10 one finds:

$$A = 1583 \text{ mm}^2,$$
$$R_s = 46.6 \text{ mm},$$
$$W_t = 37618 \text{ mm}^3,$$
$$\alpha_{ki} = 1.7,$$
$$V = 518224 \text{ mm}^3.$$

With $f = 52180$ cycles/min and $\rho = 8000 \text{ kg m}^{-3}$ we get

$$q_z = 19722 \text{ kN m}^{-1}$$

and

$$\sigma_i = 2516 N^* \text{ N mm}^{-2}.$$

For a disk made of a material with UTS = 1400 N mm^{-2} one gets:

$$N^* = 0.556$$

and from Fig. 9:

$$\varphi_{max} = 121°$$

which means that the disk will break into about three equally large pieces of 120°.

8. CONCLUSIONS

The general solution was found for the stress history in a disk after failure due to a radial crack. It was shown that immediately after cracking internal forces are built up propagating away from the crack surfaces, which are likely to cause a second failure at about 120° away from the original failure. In that way the disk breaks into three equally sized parts for which it was proven that they have the maximum translational kinetic energy of all possible failure patterns.

REFERENCES

Beitz, W. and Küttner, K.-H. (1983). *Dubbel, Taschenbuch für den Maschinenbau*, 15 Auflage. Springer, Berlin.

McCarthy, D. (1975). Definition of engine debris and some proposals for reducing potential damage to aircraft structure. AGARD-CP-186, 7.1–7.10.

Szabó, I. (1964). *Höhere Technische Mechanik*, 4 Auflage. Springer, Berlin.